Block-Copolymers Enable Direct Reduction and Structuration of Noble Metal-Based Films

Maxime Gayrard, Francois Chancerel, Maria Letizia De Marco, Denys Naumenko, Cédric Boissière, Laurence Rozes, Heinz Amenitsch, Jennifer Peron, Andrea Cattoni, and Marco Faustini*

Noble metal nanostructured films are of great interest for various applications including electronics, photonics, catalysis, and photocatalysis. Yet, structuring and patterning noble metals, especially those of the platinum group, is challenging by conventional nanofabrication. Herein, an approach based on solution processing to obtain metal-based films (rhodium, ruthenium (Ru) or iridium in the presence of residual organic species) with nanostructuration at the 20 nm-scale is introduced. Compared to existing approaches, the dual functionality of block-copolymers acting both as structuring and as reducing agent under inert atmosphere is exploited. A set of in situ techniques has allowed for the capturing of the carbothermal reduction mechanism occurring at the hybrid organic/inorganic interface. Differently from previous literature, a two-step reduction mechanism is unveiled with the formation of a carbonyl intermediate. From a technological point of view, the materials can be solution-processed on a large scale by dip-coating as polymers and simultaneously structured and reduced into metals without requiring expensive equipment or treatments in reducing atmosphere. Importantly, the metal-based films can be patterned directly by block-copolymer lithography or by soft-nanoimprint lithography on various substrates. As proof-of-concept of application, the authors demonstrate that nanostructured Ru films can be used as efficient catalysts for H_2 generation into microfluidic reactors.

1. Introduction

Due to their outstanding electronic properties and their stability, noble metals films play a key role for a variety of traditional and emerging applications. Among noble metals, those of the platinum group, present the highest thermal and corrosion resistances and high catalytic activities, arising from their partially filled d-sub-shells.[1,2] Shaped as nanoparticles they are widely used in the catalysis industry. For instance, rhodium (Rh), ruthenium (Ru), or iridium (Ir) are ubiquitous in heterogeneous catalysis, playing a crucial role in the petroleum refinement[3] and energy conversion via hydrogen generation by water electrolysis[4] or in fuel cell technology.[5] Beyond nanoparticles, Rh, Ru, and Ir play an important role in several fields if shaped as nanostructured thin films. In catalysis, supported nanostructured and nanoporous noble metal films with high surface area can be integrated in microfluidic reactors enabling running catalytic processes in a continuous way and safer conditions (i.e., in presence of toxic chemicals).[6,7] Beyond catalysis, rhodium has recently gained attention as a material for ultraviolet (UV) plasmonics with the advantages of its oxide-free nature and of the plasmon resonant modes at very short wavelengths.[8] Ruthenium films are already developed in electronics as a barrier metal for future-generation metal interconnects in logic devices and as a metal electrode for dynamic random-access memory capacitors.[9] Nanostructured Ir layers are strong candidates as mirrors and metasurfaces for space-based X-ray optics (such as telescopes) because they exhibit high reflectivity in the X-ray regime and high oxidation resistance ensuring stable performance over the lifetime of the

M. Gayrard, F. Chancerel, M. L. De Marco, C. Boissière,
L. Rozes, M. Faustini
Laboratoire Chimie de la Matière Condensée de Paris (LCMCP)
Sorbonne Université
CNRS
Paris F-75005, France
E-mail: marco.faustini@sorbonne-universite.fr
F. Chancerel, A. Cattoni
Institut Photovoltaïque d'Ile-de-France (IPVF)
CNRS UMR 9006
Palaiseau 91120, France

F. Chancerel, A. Cattoni
Centre de Nanosciences et de Nanotechnologies (C2N)
CNRS UMR 9001
Université Paris-Saclay
Palaiseau 91120, France
D. Naumenko, H. Amenitsch
Institute of Inorganic Chemistry
Graz University of Technology
Graz 8010, Austria
J. Peron
Université de Paris
ITODYS
CNRS UMR 7086
15 rue J-A de Baïf, Paris F-75013, France

2104204 (1 of 14)

ADVANCED
SCIENCE NEWS
www.advancedsciencenews.com

NANO · MICRO
small
www.small-journal.com
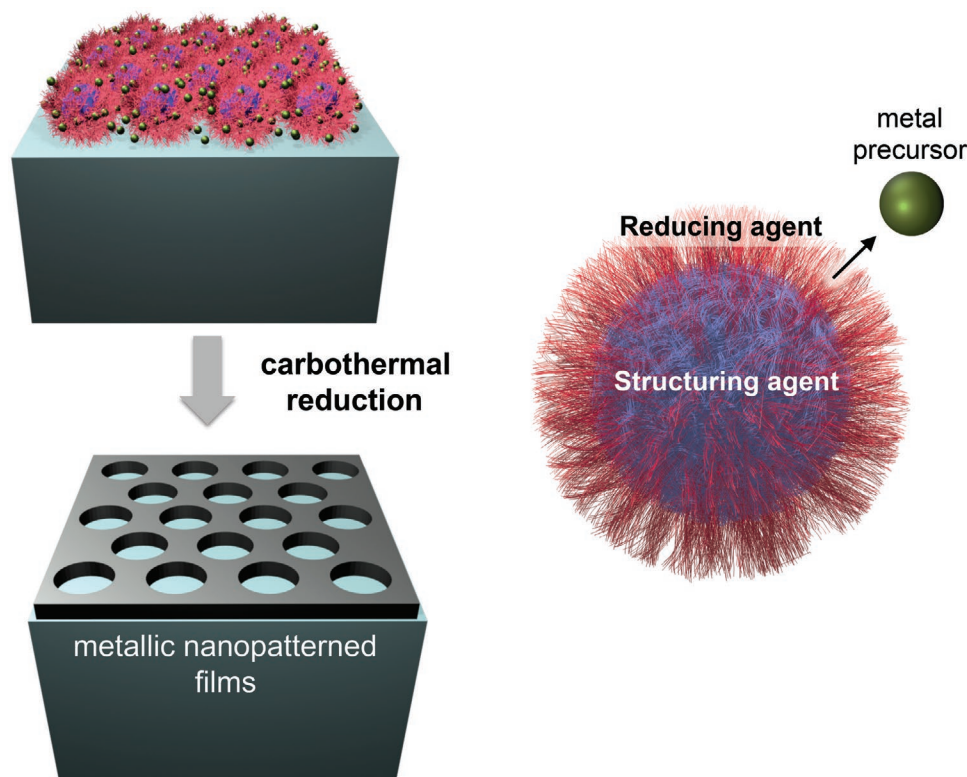
device.[10] To progress in this area, some technological challenges need to be overcome. Ru, Ir, or Rh coatings have been obtained by physical deposition (such as sputtering) or electrochemical deposition on conductive substrates. However, these processes require dedicated equipment and lack of versatility as respect to solution processing to be applied on substrates with arbitrary composition or shape. Even more importantly, structuring and patterning noble metals at the nanoscale remains a critical step, still underexplored. Classical nanofabrication schemes based on lift-off and etching are challenging due to the significant loss of materials during the process and to the intrinsic chemical stability of those metals; for these reasons, patterning methods have not been demonstrated (for Rh or Ir) or requires multi-step processes (for Ru).[11] Herein, we report a straightforward approach to obtain patterned metallic films such as Rh, Ru, or Ir directly from solution processing. The patterning and metal formation are directly obtained from films containing metal chlorides and poly(butadiene)–poly(ethylene oxide) (PB–PEO) block-copolymers micelles as structuring agent for nanolithography. Polymer and block-copolymers-assisted patterning were previously demonstrated leading to several kind of isolated and percolated metallic particles by a successive reduction of the metallic precursors.[12] Using block-copolymers as templating agents to obtain mesoporous noble films was also already reported;[13] however, this previous strategy was based on electrochemical deposition that requires a conductive substrate, a technological constraint for device fabrication.

In the present work, we overcome this limitation by proposing a new strategy to directly reduce and structure the metal containing films. We exploit the intrinsic dual functionality of the block-polymers during thermal treatment under inert atmosphere.

An example of patterning by this chemical approach is illustrated in **Scheme 1**. In this process, ideally, a hybrid film composed of a monolayer of PB-*b*-PEO micelles surrounded by metal precursors can be directly converted into nanoperforated metal-based mesh by heat treatment in inert atmosphere. Our hypothesis is that each block plays a crucial role. During the thermal treatment in mild conditions, the micelle core (PB) would act as templating agent to obtain the nanoperforations. The PEO corona, in close contact with the metal precursor, would act as a reducing agent. This assumption is guided by a rich literature indicating that PEO-based homo- or co-polymers can act at the same time as chelating agent and reducing agents in aqueous solution to form metallic nanoparticles (such as Au, Pd, and Ag).[14,15] In our approach we take inspiration from this chemistry in aqueous solution and attempt to transpose the same principle at the solid state for other noble metals (Rh, Ru, Ir). To demonstrate that, in the first part of the article, the evolution of the chemical composition, crystallinity, and nano-structure along the film preparation are investigated by a set of in situ techniques adapted to study thin films including simultaneous grazing-incidence small-angle and wide-angle X-ray scattering (GI-SAXS/GI-WAXS), X-ray diffraction (XRD), and infrared (IR) ellipsometry equipped by thermal environmental chambers. Thanks to this analytical study, we unveil an in situ reduction mechanism that involves PEO degradation and reductive carbonylation of the metallic precursors. In the second part of the article, we adapt this chemical approach to directly pattern metal-based films by micellar block-copolymer lithography

Scheme 1. Example of fabrication of nanopatterned films by in situ carbothermal reaction.

**ADVANCED
SCIENCE NEWS**

www.advancedsciencenews.com

NANO · MICRO

small

www.small-journal.com

on rigid as well as on flexible substrates. In addition, the same approach is extended to fabricate hierarchically structured metallic films by direct soft-nanoimprint lithography. In the third part, we demonstrate, for the case of Ru, that this nanostructured films can be used as efficient catalyst for H_2 generation and even easily integrated in microfluidic reactors. This new chemical route is simple, does not require electrochemical assistance nor expensive equipment or treatments in reducing atmosphere. Importantly, it is compatible with large-scale deposition and patterning. Therefore it could open perspectives for its utilization in optics, electronics/data storage,[16,17] as catalytic platform,[3] etching masks,[18] or nanoelectrodes.[19]

2. Results and Discussion

2.1. Reduction Mechanism

The chemical role of the block-copolymer and the reduction mechanism to fabricate nanostructured metallic films were investigated by combining three in situ techniques: XRD, IR ellipsometry, and GI-WAXS. To improve the sensitivity for this mechanistic study, we analyzed thick films composed of

multilayers of micelles having the same structure/composition as the one illustrated in Scheme 1 but with a higher amount of material. We illustrate the case of rhodium, an important material for catalytic and plasmonic applications.

The role of the block-copolymer as reducing agent is first investigated by in situ XRD. A schematic picture illustrating the synthetic routes toward nanostructured Rh-based films is shown in **Figure 1**. Briefly, rhodium chloride is dissolved in a solution containing water and ethanol. In the first case (Figure 1a), a film composed of the Rh-based precursor is formed by dip-coating directly from this solution. In the second case, the PB-*b*-PEO block-copolymer is added to the solution. In these conditions the PB-*b*-PEO form spherical micelles having a hydrophobic PB core and a hydrophilic PEO corona.[20] The presence of 45 nm micelles was also confirmed by dynamic light scattering. It is important that to mention no reduction takes place in the solution containing PB-*b*-PEO and the metallic precursors (even after weeks according to XRD). This stability differs from the reported examples on gold precursors that were readily reduced by the PEO-based copolymer in solution.[15] After dip-coating, we obtain a hybrid mesostructured films composed of micelles surrounded by Rh precursors. As reported in previous studies, since the metallic precursors are
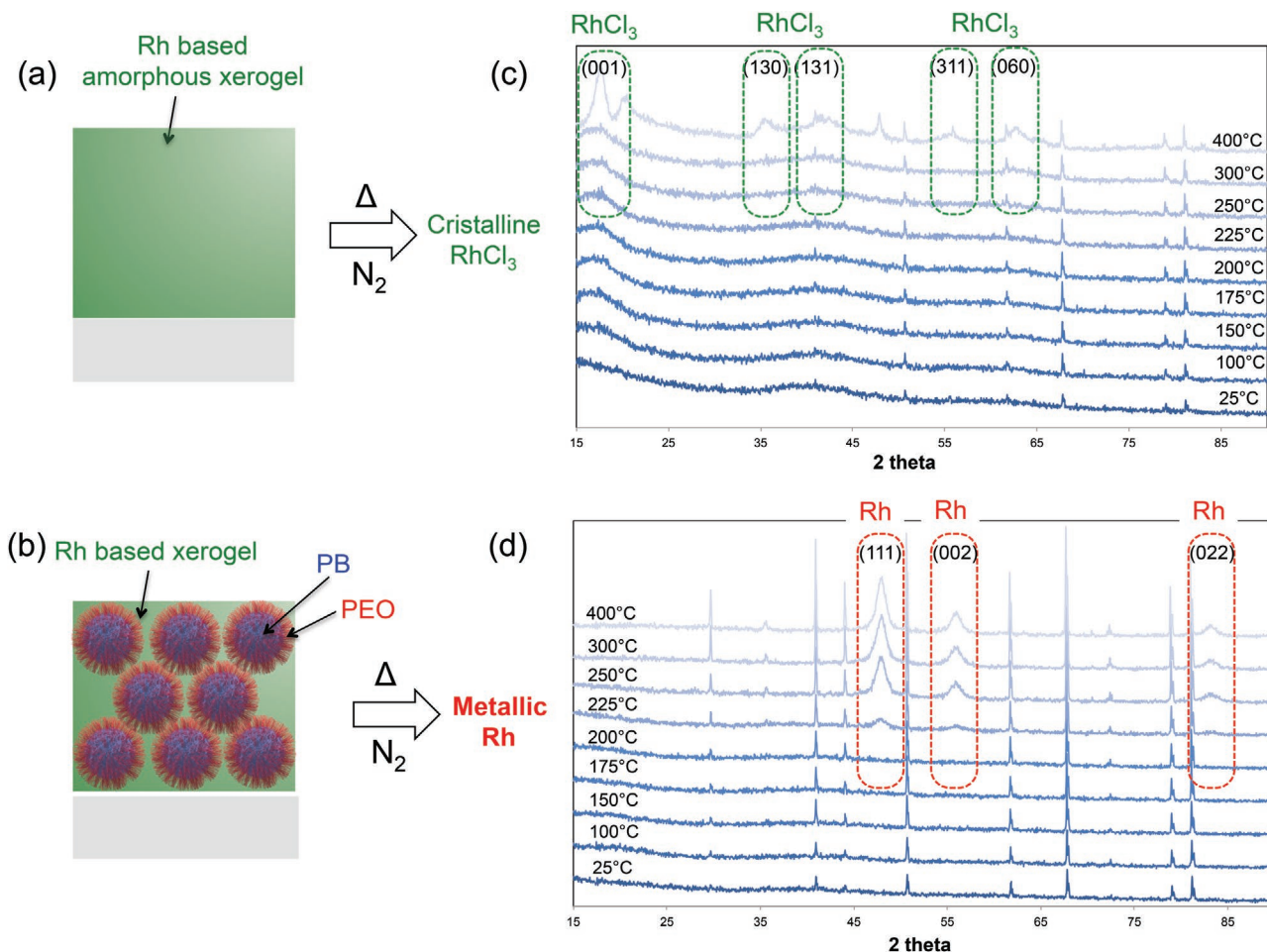

Figure 1. a,b) Illustration of the dip-coated Rh-based films without and with PB–PEO micelles, respectively. c,d) In situ XRD diffractograms during the thermal treatment of the Rh-based films without and with PB-*b*-PEO micelles, respectively. The nonindexed peaks correspond to the substrate.

ADVANCED
SCIENCE NEWS
www.advancedsciencenews.com

NANO · MICRO
small
www.small-journal.com

soluble in polar solvents they are mostly located in the PEO corona and are not likely to migrate into the PB core.[21,22] The dip-coating process was performed in controlled atmosphere to keep the relative humidity below 10%.[23] Both films were analyzed by in situ XRD during the thermal treatment under inert atmosphere (N_2).

Figure 1c,d reports the evolution of the diffractograms as function of the temperature of the Rh-based films without and in presence of the PB-*b*-PEO micelles. In both cases at 25 °C, no Rh-related diffraction peak is visible, indicating that after the dip-coating, the films are amorphous xerogels. In presence of PB-*b*-PEO (Figure 1d), diffraction peaks characteristic of the metallic Rh fcc structure appear at 225 °C.

The XRD peaks are very broad corresponding to a size of crystallites of 8 nm as determined with the Scherrer equation.[24] With temperature increasing beyond 225 °C, the intensity of the peaks further increases as a consequence of further crystallization. In contrast, XRD patterns of the sample prepared without PB-*b*-PEO do not present any metallic Rh fcc peak in the same temperature range (25–300 °C) (Figure 1c). Above 300 °C, broad peaks appear characteristic of the $RuCl_3$ crystals. The appearance of unindexed peaks at high temperatures is associated with the silicon substrate which becomes more and more exposed upon shrinkage of the investigated layers.[2] This first series of experiments confirms that the presence of block-copolymer is needed to reduce the Rh^{3+} precursors and that the reduction is taking place at relatively low temperature, around 225 °C.

The reduction mechanism during the thermal treatment under inert conditions was further studied by different in situ techniques. **Figure 2** displays side by side the evolution of the chemical composition and crystallinity obtained by in situ IR ellipsometry and GI-WAXS as function of the temperature performed on two different samples prepared in the same conditions. Both techniques were chosen since they are well adapted to characterize thin films. The in situ GI-WAXS was conducted at synchrotron since it provides a better time (and temperature) resolution compared with in situ XRD analysis.

We first analyze the evolution obtained from IR ellipsometric data of Figure 2a. During an ellipsometric experiment, IR polarized light beam interacts with the film on a Cr-coated Si substrate (reflective in the IR range). This interaction changes the state of polarization of the reflected light. Measurements of the initial and final states of polarization lead to the determination of the transformation properties of the system which may be parametrized by the interference amplitude component Ψ and the phase difference Δ. Both Ψ and Δ values are very sensitive to photons absorptions due to vibrational modes at IR wavelengths. In our experiments, we show the Δ spectra that give a better insight of the chemical changes in the material during annealing. The Δ spectrum at 25 °C presents many different features in Figure 2a. The large bands centered at ≈1650–1670 cm^{-1} and at 3200 cm^{-1} can be attributed to the presence of water molecules in the film, either due to residual water from the micellar solution and/or due to humidity sorption from atmosphere.[25] These bands disappear at 100 °C indicating that the water was fully desorbed at this temperature. The band at 1070 cm^{-1} can be attributed to the stretching of the C−O−C bonds in the PEO.[25,26] The stretching of the

C−O−C bonds characteristic of PEO functions is usually observed close to 1100 cm^{-1}. In our case, this stretching is red shifted to 1070 cm^{-1}, very probably due to the complexation of Rh(III) cations by oxygens of PEO chains.[27] Bands in the range 2850–2920 cm^{-1} correspond to the symmetric and asymmetric stretching of C−H.

Above 100 °C, the signal corresponding to the C−O−C stretching disappears, which may indicate that the PEO block starts decomposing/reacting. Previous studies for the thermal decomposition of PEO under inert atmosphere showed that the onset of decomposition in N_2 is at ≈180 °C, and that the decomposition is not complete up to 400 °C.[26] The products of the thermal decomposition of PEO under inert atmosphere are ethanol, methanol, formaldehyde, acetyl aldehyde, CO, H_2O, and CO_2.[26] The decomposition of the PEO at lower temperatures observed in our experiment is another indication that Rh species might interact with PEO. Moreover, at 150 °C a new signal appears at 2090 cm^{-1}. Several studies report that in the presence of H_2O, CO can react to $RhCl_3$ physisorbed onto a surface. The Rh^{3+} is reduced by CO, and forms the dimer $[Rh(CO)_2Cl]_2$ (IR peaks at 2089 and 2033 cm^{-1}).[28,29] This reaction is called reductive carbonylation, and occurs also in absence of water.[28] The signal at 2090 cm^{-1} increases in intensity at 200 °C, and another band at ≈2030 cm^{-1} appears. These two bands match well with the symmetric and asymmetric stretching of gem-dicarbonyl species. In this complex, the rhodium is monovalent.[30] These two signals are observed up to 225 °C, and are no longer present at 250 °C. This might be due to the fact that at high temperatures (above 225 °C), reductive desorption of CO occurs and Rh(I) is further reduced to Rh(0).[31] This is in agreement with the in situ GI-WAXS analysis presented in Figure 2b in which we highlight the evolution of the (111) diffraction peak of the metallic Rh nanoparticles as function of the temperature. The analysis indicates that formation of metallic rhodium starts at 220–225 °C confirming a possible two steps reduction process as illustrated in Figure 2c: i) starting from 150 °C, the reduction from Rh(III) to Rh(I) through the formation by a carbonyl intermediate; it is important to notice that the presence of intermediates was not observed by XRD or GI-WAXS suggesting that the carbonyl intermediate does not form a crystalline entity; ii) from 225 to 250 °C reduction from Rh(I) to Rh(0) by the carbon monoxide. This mechanism is different from a previous report in which Ir^{3+} precursors were reduced to metallic Ir in a single step by PMMA at temperature >300 °C due a depolymerization-induced radical process.[2]

In contrast, the peaks at higher wavenumbers (≈2850–2920 cm^{-1}) characteristic of C−H bonds and attributed to remaining PB chains do not vary significantly up to 300 °C but disappear above 350 °C. To gain a better understanding on the evolution of the system during the thermal treatment, we also performed in situ UV–vis–NIR spectroscopic ellipsometry (190–1700 nm) to monitor the thickness contraction during the thermal treatment. The evolution shown in Figure S2, Supporting Information, is characterized by several contractions that can be identified accordingly with the IR ellipsometry data: a first 35% contraction between 50 and 100 °C is attributed to the loss of volatile H_2O; a second 15% volumetric contraction between 100 and 200 °C can be attributed to the PEO decomposition; a sharp 25% contraction between 200 and
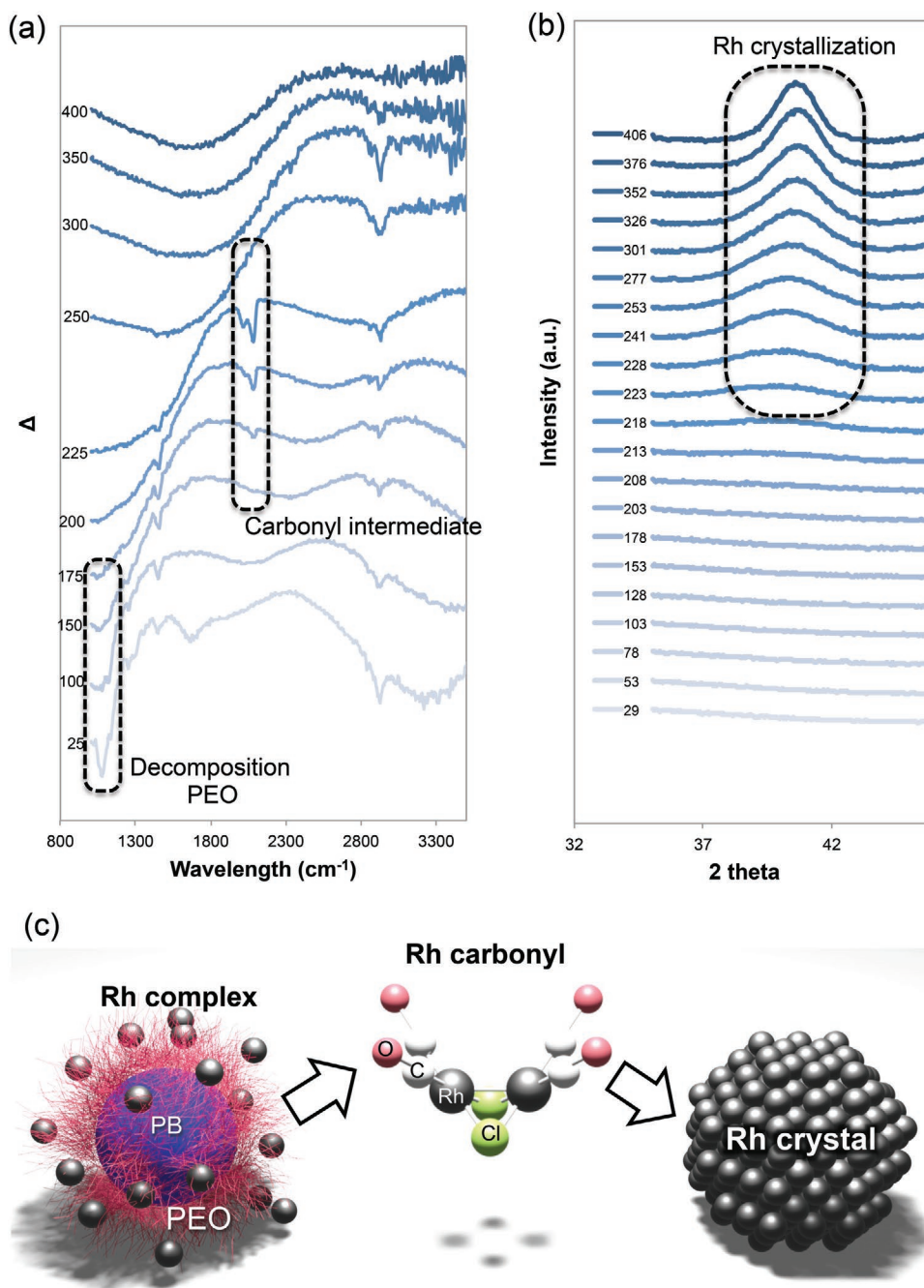
Figure 2. a) In situ spectroscopic IR ellipsometry: evolution of phase shift difference (delta) as function of the calcination temperature. b) In situ GI-WAXS patterns as a function of the calcination temperature. c) Schematic illustration of the Rh chemical transformations.

250 °C correspond to the Rh reduction (with the Cl loss). After 250 °C, the film contracts probably due to the progressive decomposition of the PB block. To confirm that, we also performed energy dispersive X-Ray analysis on the Rh/PB-*b*-PEO samples treated between 200 and 400 °C in inert atmosphere (Figure S2, Supporting Information). Between 200 and 400 °C the carbon content decreases significantly due to the PEO and PB degradation (as observed by IR ellipsometry). At 400 °C some residual carbon remain (C/Rh = 0.3) but no characteristic peaks of PB were observed by IR ellipsometry. Determining

the chemical nature of the residual organic species on thin films treated above 400 °C is challenging by alternative ex situ methods (such as XPS) due to the atmospheric contamination. However, according to the literature the residual organic species can be unreacted PB (not detectable by IR), graphitic carbon, or adsorbed CO/CO_2.[2]

All these analyses indicate that: i) the presence of the block-copolymer is needed for the carbothermal reduction; ii) while we cannot exclude that both blocks can participate in the reduction reaction, PEO is the more probable candidate. Indeed PEO

**ADVANCED
SCIENCE NEWS**

www.advancedsciencenews.com

NANO · MICRO
small

www.small-journal.com

decomposes at lower temperature to form a reduced Rh-based intermediate compound that is further reduced into metal-based Rh; iii) residual carbon-based species (unreacted polymer or products of reaction) remain in the structure.

2.2. Structural Evolution

The structural evolution of mesostructured films during the reduction process was investigated by combining ex situ SEM and in situ GI-SAXS during thermal treatment under inert atmosphere. Three main structural features can be identified and they will be named as I, II, and III in the following sections. **Figure 3**b represents a series of SEM micrographs of the film at various characteristic stages of the thermal treatment. The samples calcined at 150 and 190 °C correspond to the films before and during carbonylation. Both films present similar structure with a thickness of ≈60–70 nm and pores at the surface having size of ≈15–20 nm (structure I). The SEM micrograph at 300 °C shows the film after reduction (structure II). Two main structural modifications can be observed: a thickness contraction, and the appearance of sub-10 nm Rh nanoparticles composing the pore's walls. At 400 °C, the porous structures are lost and the films are composed of isolated Rh nanoparticles (structure III) with broad size distribution.

To have a complete view of the evolution between the different structures, temperature-resolved GI-SAXS was conducted. Figure 3c shows characteristic GI-SAXS 2D patterns of the Rh-based film at different temperatures. In addition the structural evolution was investigated by integrating the signal intensity along the in-plane and out-of-plane directions as a function of the temperature as displayed in Figure 3d,e.

The GI-SAXS pattern at 25 °C (Figure 3c) displays two symmetrical diffraction signals close to the beam-stop. These signals extend in the z direction while becoming less intense, before completely disappearing behind the beam-stop, which is typical of the loss of ordering in directions normal to the surface.[32] The diffraction signal at $q_y = 0.13$ nm^{-1} correspond to a characteristic in-plane periodicity of 48.3 nm which is in agreement with the mean pore center to center distance observed by SEM. Increase of the temperature up to 225 °C does not modify significantly the diffraction signal (it is slightly more elongated in the z direction due to film contraction).[33]

By contrast, a clear structural transition between structure I and II is taking place between 225 and 250 °C, simultaneously with the reduction and crystallization of the metal nanoparticles (as observed by GI-WAXS). The GI-SAXS patterns at 253 and 301 °C display elongated diffracted spots that are displaced toward higher values of q_z (Figure 3e). The elongation of the signal in z direction of the reciprocal space is characteristic of a strong increase in pores anisotropy induced by an out-of-plane contraction of the film concomitant to the reduction of the metal carbonyl. The displacement of the signal toward higher q_z is more unusual for mesostructured films obtained by micelles templating. To explain this effect it must be mentioned that, for this investigation, the initial thickness of the film is below 100 nm corresponding roughly to a bilayer of micelles (visible on Figure 3b). Upon reduction, the displacement of the q_z to higher values could be accounted for the fact

that the predominant signal comes from the surface porosity that is located above the interface with the substrate. This particular feature will be further discussed for the case of other metals and by correlation with SEM microscopy. Beyond this, it is important to emphasize that the mesostructure is preserved after reduction and crystallization (as observed in the SEM of Figure 3b).

After 325 °C, the transition between structures II and III (mesoporous film to dots) occurs. This transition can be visualized in the GI-SAXS patterns at 352 and 406 °C in Figure 3c. This progressive evolution is characterized by a decrease of q_z values (Figure 3e). In addition starting from 352 °C, an additional peak at higher q_y appears (Figure 3d) indicating the formation of small Rh nano-objects progressively replacing the porous structure. The new signal progressively grows and broadens toward lower values of q_y as the temperature increases. As shown in Figure 3c the broad and intense GI-SAXS signal at 406 °C is in agreement with the presence of isolated polydispersed Rh nanodots lying onto the surface (structure III) as observed in the SEM micrograph of the film calcined at 400 °C in Figure 3b. It is interesting to correlate this result obtained by in situ GI-SAXS with the in situ IR ellipsometric analysis discussed in Figure 2b. It is worth mentioning that the loss of the mesoporous metallic structures above 325 °C is concomitant with the disappearance of the peak at higher wavenumbers (≈2850–2920 cm^{-1}) characteristic of the methylene groups of the PB block. One can thus hypothesize that the residual organic matter still present in the material after crystallization might have a role in stabilizing the mesostructure in the case of metallic rhodium. The combination of all these in situ analyses allows proposing a schematic view of the mechanism of formation and evolution of mesostructured Rh-based films. All the aforementioned transitions can be summarized in the scheme in Figure 3a. In the case of rhodium, each block of the block-copolymer micelles plays a specific role of reducing and structuring agent. Now, is this process generalizable to other noble metals? To answer this question, we have performed a similar analysis with two other elements: ruthenium and iridium. Briefly, as in the case of Rh, films were obtained by dip-coating solutions containing IrCl$_3$ or RuCl$_3$ in presence of PB-b-PEO onto a silicon wafer. Their evolution was followed in situ by simultaneous GI-SAXS and GI-WAXS measurements during thermal treatment under inert atmosphere. **Figures 4**a and 4c show the evolution of the GI-WAXS spectra as a function of the temperature for Ru- and Ir-based films, respectively. In both cases the metallic phase is obtained.

The WAXS diffraction peaks characteristics of the metals appear around 275 °C for both ruthenium and iridium. The macroscopic appearance of the materials obtained by this method is typical of a metallic film. As an example, **Figure 5** displays a photograph of a metallic mesoporous Ru-based film covering a glass substrate obtained at 300 °C. The GI-SAXS patterns at various temperatures are shown in Figures 4b and 4d for Ru and Ir, respectively. As for Rh, three main characteristic structures can be observed (I, II, and III). At 25 °C, the diffraction patterns confirm the presence of the organic/inorganic mesophase (structure I). These diffraction signals are centered at $q_y = 0.15$ nm^{-1} and $q_y = 0.072$ nm^{-1} for Ru and Ir, respectively, and correspond to a characteristic lateral
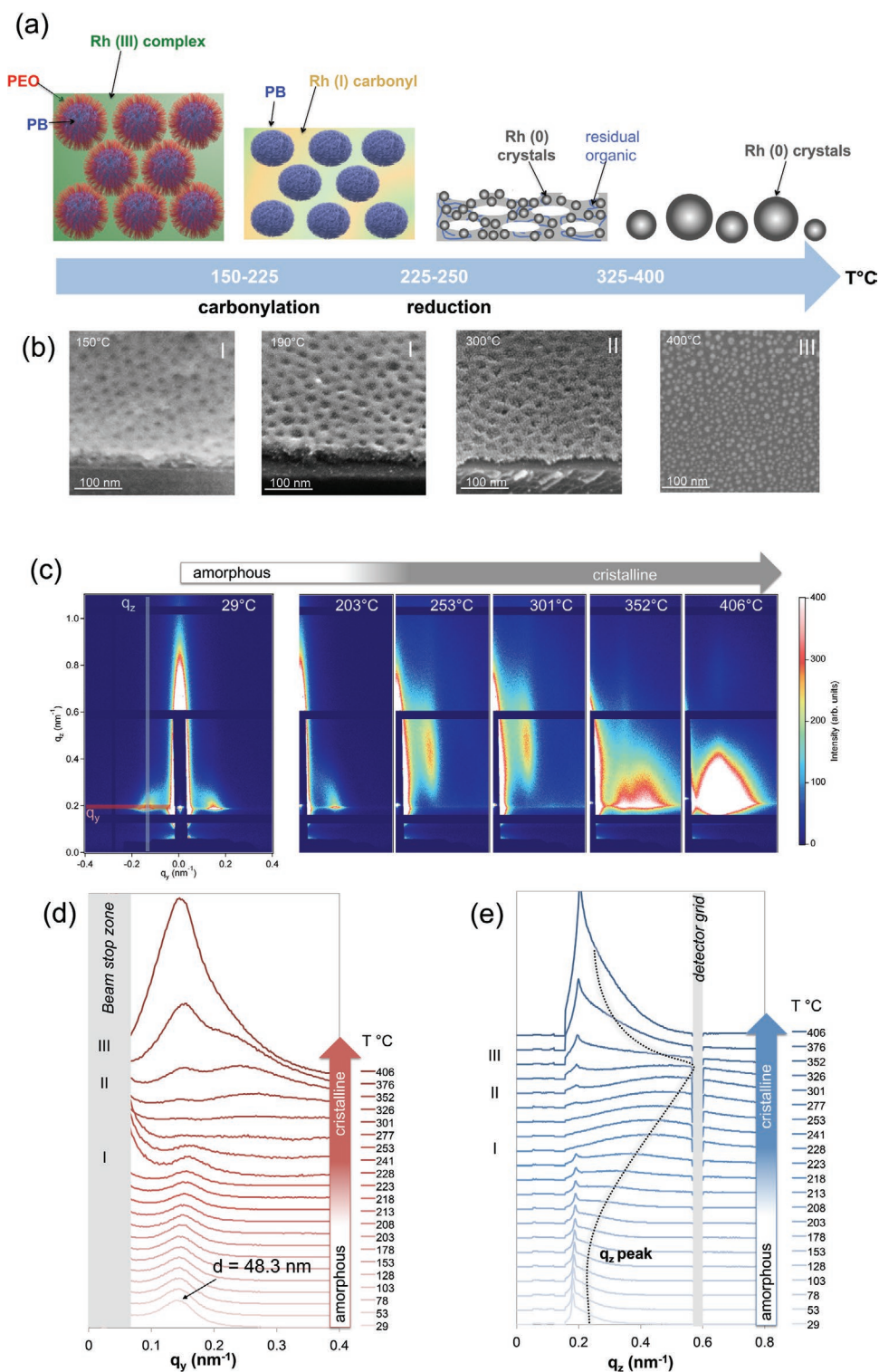
Figure 3. a) Illustration of the proposed mechanism of formation and structural evolution of the Rh-based films. b) SEM micrographs of the films treated under N_2 at increasing temperature. c) In situ 2D GI-SAXS patterns of the films during the thermal treatment. d,e) Evolution of the integrated intensity along q_y and q_z as indicated in (c) at 29 °C; dotted line in (e) is guide to the eye.

periodicity of 42 and 87 nm, respectively. After crystallization, above 275 °C we observe the elongated 2D patterns at higher q_z characteristic of the structure II. The presence of mesoporous

networks is confirmed in the cross-sectional SEM view of the metallic films calcined at 300 °C as shown in Figure 4e,f. A top-view SEM micrograph of the Ru film is also displayed in
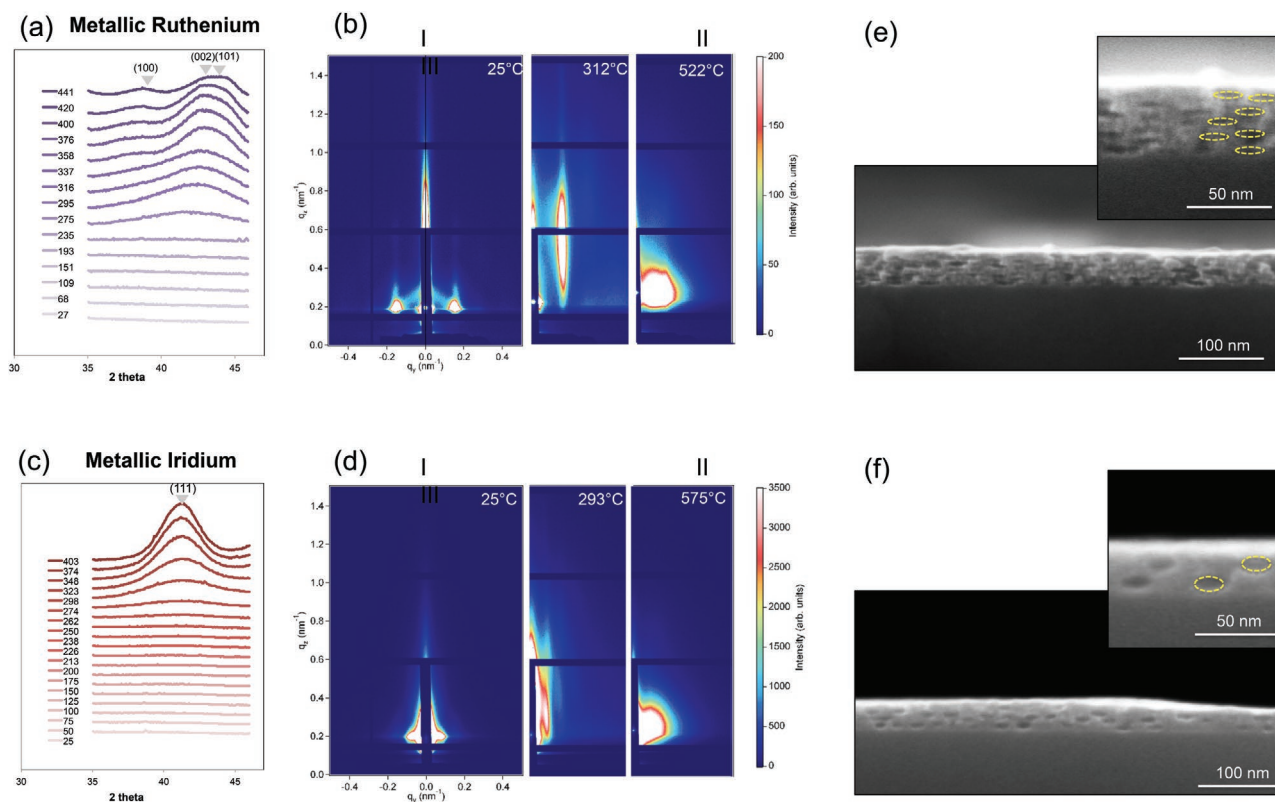
**ADVANCED
SCIENCE NEWS**

www.advancedsciencenews.com

NANO · MICRO

small

www.small-journal.com

Figure 4. a,c) In situ GI-WAXS during thermal treatment in N_2: evolution of the spectra of the Ru- and Ir-based films, respectively. b,d) In situ GI-SAXS during thermal treatment in N_2: 2D GI-SAXS patterns at three representative temperatures of Ru and Ir films, respectively. e,f) Cross-sectional SEM micrographs of the mesoporous Ru- and Ir-based films, respectively obtained at 300 °C.

Figure S3, Supporting Information. Both films display elliptical mesopores having larger diameter of around 15–20 nm; the mesoporous Ir film present a lower density of pores in agreement with the previous analysis on the pore distance based on the integration along q_y. The origin of this denser structure remains unclear. This can be attributed to a lower amount of micelles formed in presence of Ir precursors. At higher temperature (above 400 °C), the broad intense signal in the GI-SAXS patterns (Figure 4b,d) characteristic of the formation of

isolated Ru or Ir metallic nanoparticles appears (as structure III observed for Rh).

2.3. Metal-Based Nanomeshes by Block-Copolymer Lithography

Guided by the aforementioned analysis, we adapted the approach of using block-copolymer micelles to simultaneously reduce and structure noble metals for nanolithography at the sub-20 nm scale as shown in Scheme 1. This patterning method was already developed for metal oxides such as TiO_2[16,20] or ITO[34] but never demonstrated for metallic materials so far. The process is illustrated in **Figure 6**a. The PB-*b*-PEO block-copolymer was first dissolved in a hydro-alcoholic solution in presence of the metallic precursors. A film is then obtained on the silicon substrate by dip-coating from this solution. As respect to the previous experiments, the deposition conditions were adjusted to obtain a monolayer of micelles that are surrounded by the metallic precursor. By following the same protocol described in the previous sections, the films were then heated at 300 °C under N_2 to reduce the precursors into metallic particles. The SEM micrograph in Figures 6b and 6c shows the Rh- and Ru-based patterned films onto silicon, respectively. The films are composed of meshes having perforations with diameter of ≈20 nm and periodicity of ≈50 nm in agreement with the previous GI-SAXS analysis. One of the main advantages of the method is that the metallization does not require any external
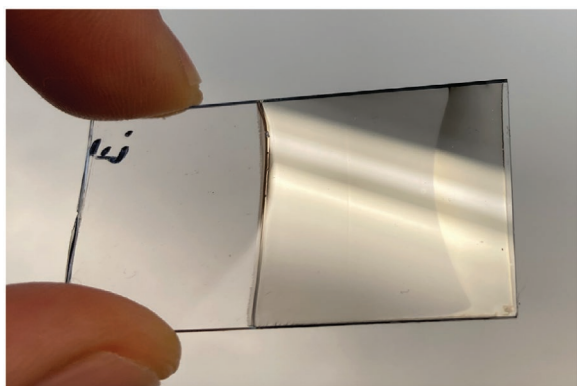

Figure 5. Photograph of the dip-coated mesoporous Ru-based film obtained at 300 °C.
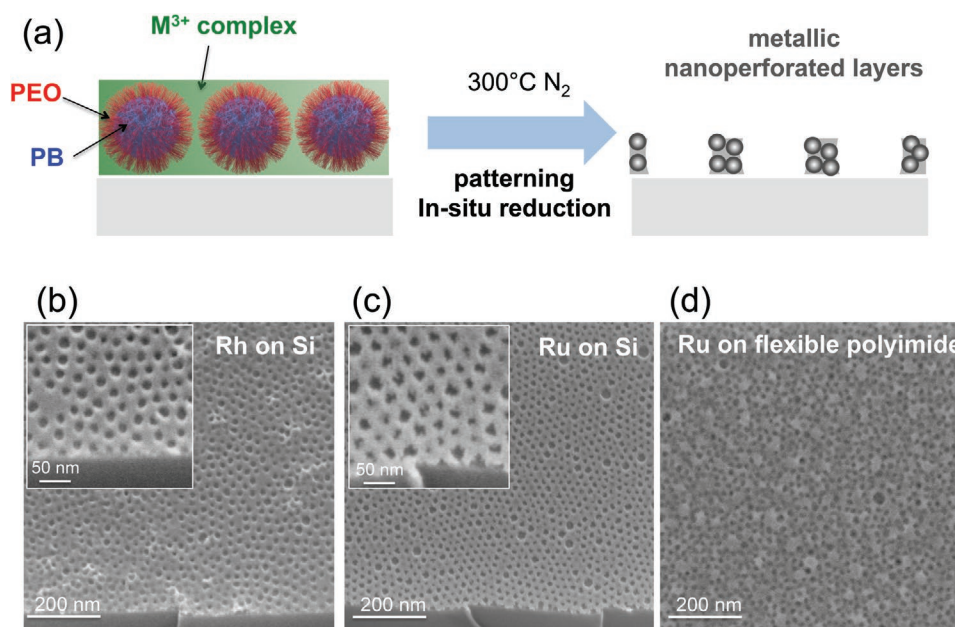
Figure 6. a) Illustration of the patterning process to obtain metal-based nanomeshes by block-copolymer lithography. b,c) Rh- and Ru-based nanomeshes on silicon. d) Ru-based nanomesh on a flexible polyimide substrate.

reducing agent or conductive substrate. Consequently direct metal nanopatterning can be envisioned on any substrates with moderate thermal stability. One example is shown in the SEM micrograph of Figure 6c in which the Ru nanomesh exhibiting well-defined perforations could be obtained on a flexible polyimide substrate, that is known to be thermally (and chemically) stable.

2.4. Patterned Metal-Based Films by Soft-Nanoimprint Lithography

To confirm the versatility of the approach we demonstrate the fabrication of metal-based nanostructured films by direct soft-nanoimprint lithography from hybrid block-copolymer/precursors films. A schematic illustration of the process is reported in **Figure 7**a. The film is applied by dip-coating deposition from the hydro-alcoholic solution containing the metallic precursors and the block-copolymer micelles. The initial film thickness after dip-coating was ≈100 nm as determined by spectroscopic ellipsometry. After evaporation of the solvent, the film is immediately embossed by patterned PDMS-based stamp previously degassed in vacuum. This method, called degassing-assisted patterning,[35] allows improving the replication of the embossed nanostructures.[36] The layer is stabilized at 130 °C before demolding. This imprinting process is pressure-less, does not require any imprinting equipment and can be realized on large scale and on arbitrary substrates.[37]

Figure 7b displays the SEM-FEG micrograph of the rhodium-based patterned films after thermal treatment at 300 °C. The film is composed of arrays of squared perforations at the submicrometric scale. The inset in Figure 7b displays the picture of a patterned sample of 4 cm² exhibiting areas with different iridescent colors characteristic of diffractive gratings

with periodicities ranging from 400 to 1000 nm.[38] To prove the versatility of the technique, the same patterning strategy was demonstrated on flexible polyimide substrate. Figure 7c displays the optical images of the sample before and after reduction. The presence of the Rh pattern after reduction was also confirmed by atomic force microscopy as shown in Figure 7d. Similarly, metallic Ru nanostrucures were obtained by direct soft-nanoimprint lithography (**Figure 8**a). Figures 8c–8e display a higher magnification SEM micrographs of arrays of squared hole with periodicity of 800, 500, and 400, nm respectively. In all the cases, the presence of the mesopores of ≈20 nm is clearly visible on the surface and also in cross-sectional images (Figure 8b) in agreement with the previous observations for nonpatterned films.

2.5. Catalytic Hydrogen Generation and Integration in Microfluidic Reactors

As proof of concept of application, we explored the viability of our nanostructured films for the catalytic hydrolysis of sodium borohydride ($NaBH_4$) for H_2 production. Among chemical hydrides, $NaBH_4$ is a promising sustainable hydrogen storage system that can provide H_2 "on-demand" for proton exchange membrane fuel cells.[39] The overall conversion of $NaBH_4$ via the self-hydrolysis is very low and catalysts are needed. In this context, ruthenium-based catalysts are known to be the most efficient materials for H_2 generation from $NaBH_4$. For this study, we thus considered the mesoporous Ru-based films prepared by carboreduction of block-copolymers micelles at 300 °C (as in Figure 4e). In this case, to increase the amount of catalyst on the surface, the film was drop-casted on the silicon wafer to obtain a thick film composed of 0.58 mg of metallic mesoporous Ru-based materials.
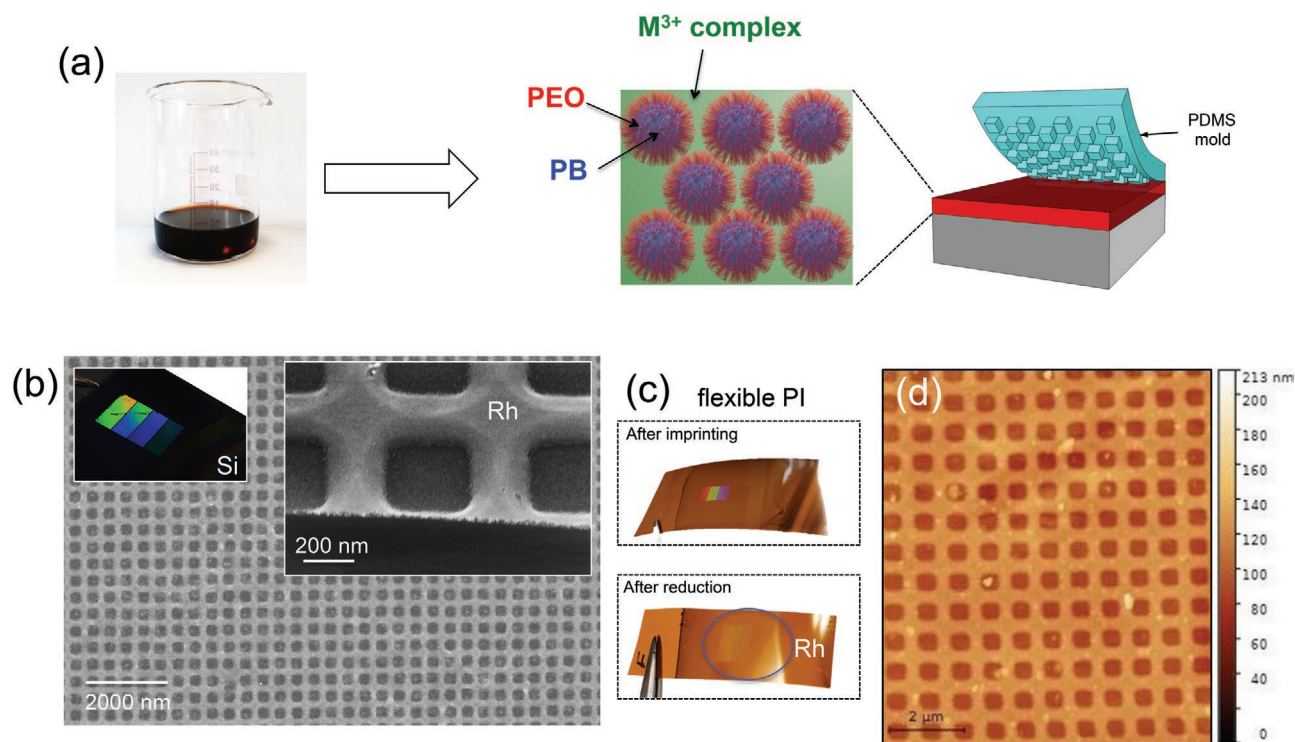
Figure 7. a) Scheme of the patterning process of the metal-based films by direct soft-nanoimprint lithography. b) SEM micrograph of Rh-patterned film on silicon (inset optical image of the patterns and SEM at higher magnification). c) Optical image of the Rh-based film on flexible PI substrate before and after reduction and d) corresponding AFM micrograph.

In a first experiment, the activity of the films was first tested in a standard batch reactor at 20 °C in conditions comparable with the literature. The system contains an aqueous solution with 4%w $NaBH_4$ and 4%w of NaOH. Since $NaBH_4$ solutions are unstable (the self-hydrolysis reactions can occur at low pH conditions), NaOH is usually added to increase the pH and stabilize the solution.[40] The hydrogen evolution was probed by flow-meter. The plot in **Figure 9**a displays the volume of H_2 generated as function of the time. The plot presents a characteristic pseudo-linear trend that can be fitted to determine the activity of the catalyst that corresponds to 19 843 mL_{H2} g^{-1} min^{-1}. This value was compared with those of other Ru-based catalysts reported in the literature and obtained in similar conditions (3–5%w of NaOH). Figure S4, Supporting Information, displays the plot of the activity of the Ru-based catalysts as function of the % $NaBH_4$ in the solution since the activity generally increases with the %w $NaBH_4$. Notably, our mesoporous Ru-based catalyst shows an excellent activity compared to other catalysts tested in similar conditions and matches the performances of the best catalyst but obtained with a solution containing 10%w $NaBH_4$. It is important to specify that the sample is characterized by a relatively high surface area of 114 m^2 g as measured by N_2 physisorption (BET analysis) on a powder dried from the same solution and treated in the same conditions of the sample used for the catalytic test.

In a second experiment, we demonstrated that the Ru-based mesoporous films can be integrated in microfluidic reactors to perform H_2 generation, "on-demand" and in a continuous

way. As reported in many articles in the literature, compared to conventional batch reactions, utilization of microreactors offers several advantages: i) they enable running processes in a continuous way, ii) microfluidic reactors allow efficient heat and matter transport often leading to enhanced efficiency and selectivity, iii) due to the small volumes involved, they are better suited in presence of toxic and or explosive chemicals[7] (such as $NaBH_4$), and iv) they enable multistep chemical processes and multi phases (liquid/liquid, gas/liquid, solid/liquid) exchanges.[41] To be integrated in microchannels, the catalyst needs to be immobilized[42] or supported as "fixed-bed" film.[7] The fabrication scheme is illustrated in Figure 9b. A stripe (width ≈ 0.6–1 mm) of mesoporous Ru-based films was obtained by dip-coating the entire surface and removing manually the excess of the film simply by wiping with an absorbent paper (before calcination). After calcination and reduction, the Ru/glass substrate was covered by a PDMS channel having a Y geometry with a channel width of 600 μm. As show in the photograph in Figure 9b, this configuration enables controlling independently the flow in the reactive zone (Ru stripes) with water (as reference) or the reactive 4% $NaBH_4$/4% NaOH solution. The H_2 generation in the microchannel was followed by optical microscopy. As shown in the Video S1, Supporting Information, and the optical micrographs in Figure 9d when the $NaBH_4$/NaOH solution reaches the Ru reactive zone, H_2 bubbles form and lay on the Ru or the PDMS surface. After reaching sufficiently large size (by growing and coalescing), they are transported with the flow toward the outlet of the reactor. Despite the simplicity of the approach, this experiment
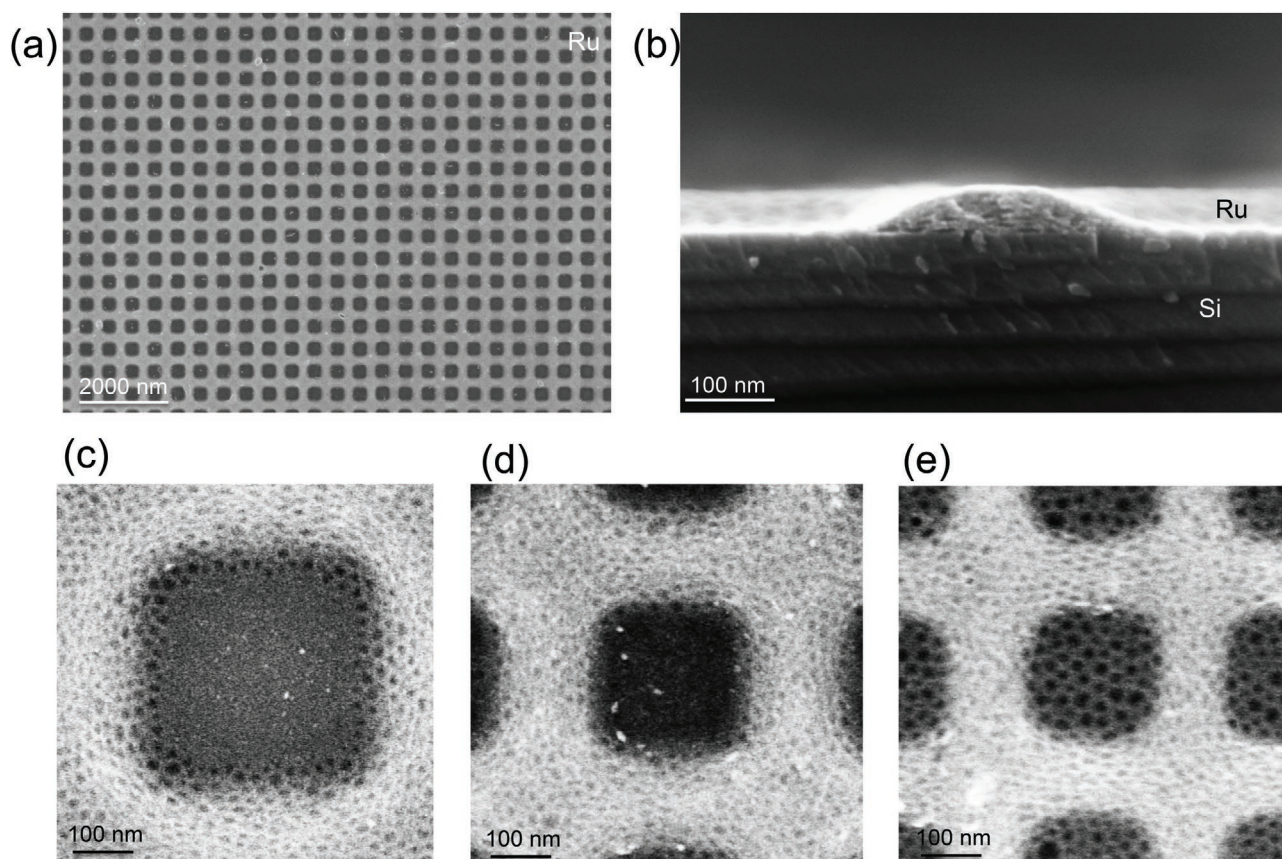
Figure 8. a,b) Top-view and cross-sectional SEM micrograph of Ru-based patterned film. c–e) Higher magnification top-view micrographs of arrays of squared hole with periodicity of 800, 500, and 400 nm, respectively, made of mesoporous Ru-based materials.

proves the potential for the supported nanostructured noble metal films to be easily integrated in catalytic devices. In perspective, this approach might allow designing even more sophisticated microfluidic reactors including multicatalytic zones and gas-exchange systems.[41]

3. Conclusions

In conclusion, we have developed a method to fabricate nanostructured metal-based films composed of Rh, Ru, or Ir and residual organic species by solution processing. From a
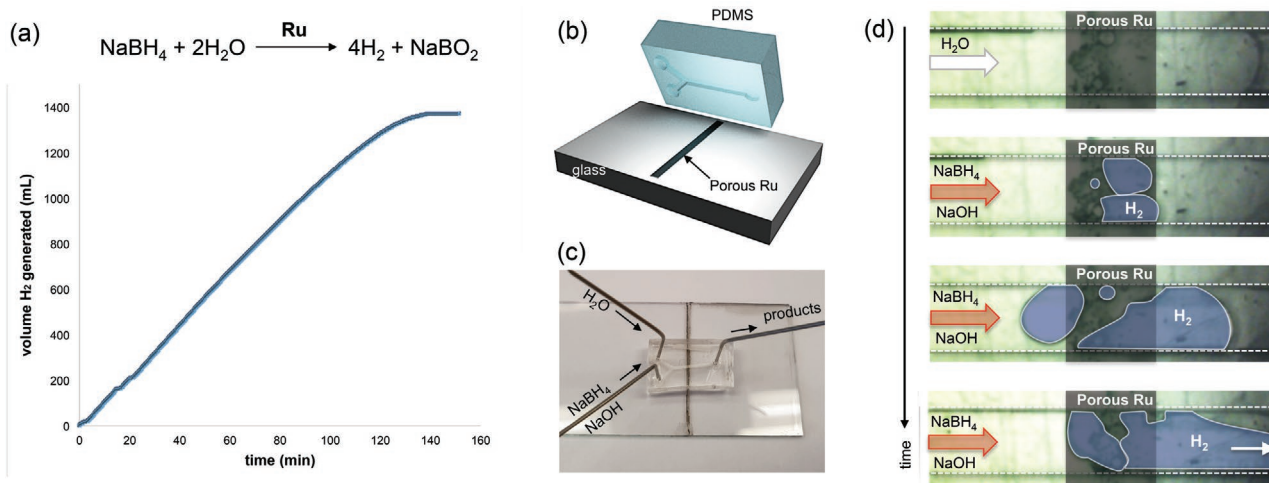

Figure 9. a) Evolution of the volume of H_2 as function of the time for a reaction catalyzed by a mesoporous Ru-based film. b) Illustration of the fabrication process to obtain the microreactor. c) Photograph of the microreactor. d) Optical micrographs versus time showing the H_2 bubbles generation into a microchannel (false colors were added to improve the visibility).

synthetic point of view, we propose to exploit the dual functionality of the block-copolymer PB-*b*-PEO micelles that act both as templating and reducing agents. In previous reports, block-copolymers were used as templating agents. It was also reported that polymers could act as reducing agents. In this study, we combine the two functionalities in a single molecule. Additionally, from the fundamental point of view, we provide new understanding on the reduction mechanism occurring during carbothermal processes, a relatively underexplored field. A set of in situ techniques has allowed capturing the carbothermal reduction mechanism occurring at the hybrid organic/inorganic interface, unveiling the formation of a carbonyl intermediate. The process presents several advantages; it is simple, it is scalable, does not require any external or dedicated equipment reducing agent and can be applied by solution-processing on substrates of various shape and composition (stable at mild temperatures). Furthermore, this chemical approach enables the challenging patterning of noble metal-based films directly by micellar block-copolymer lithography and by soft nanoimprint lithography. At last, we showed that mesoporous Ru-based films are excellent catalysts for H_2 generation and can be easily integrated in microreactors to carry out reactions in a continuous manner. From a fundament point of view, this work expands the synthetic toolbox in nanomaterials fabrication by using organic template acting also as reducing agents.

We also believe that this report will trigger new fundamental research on the synthesis of nanostructured metallic films by chemical methods providing new possibilities for device fabrication at low cost.

4. Experimental Section

Chemicals: The metallic precursors were rhodium (III) chloride hydrate (RhCl$_3 \cdot x$H$_2$O, Rh 38.5–45.5%, Alfa Aesar), ruthenium(III) chloride hydrate (RuCl$_3 \cdot x$H$_2$O, Sigma Aldrich), iridium(III) chloride hydrate (IrCl$_3 \cdot x$H$_2$O, Alfa Aesar); and the PB–PEO (Mn = 5600 g mol^{-1} PB and 10 000 g mol^{-1} PEO [polydispersity index = 1.05]) was provided by from Polymer Source. 6 inch-diameter p-type (100) Si wafer with a resistivity of 1–10 ohm cm was purchased from Siltronix Silicon Technologies. The polyimide sheet (304 mm × 200 mm × 0.075 mm) was purchased from Radiospare.

Preparation of the Films: At first, 0.020 g of PB–PEO was dissolved in a EtOH/H$_2$O (7/1 w/w) solution. To induce complete dissolution of the block-copolymer, the solution was warmed at 70 °C for 30 min. After cooling, 0.122 g of salt metal precursor was added to the solution. The silicon wafer and the polyimide sheet were cleaned with ethanol solution and oxygen plasma. The substrate was coated via dip-coating performed in a controlled atmosphere (at relative humidity < 10% and room temperature). To obtain thick multilayer films for the in situ investigations and for nanoimprint lithography the films were obtained by dip-coating at 10 mm s^{-1}. To obtain monolayer of micelles the films were dip-coated at 0.7 mm s^{-1}.[22]

Soft-Nanoimprint Lithography: *Master and PDMS-based stamp fabrication*: The silicon master mold was fabricated by electron beam lithography at 100 KeV (Vistec 5000+) and reactive ion etching. An A7 PMMA positive-tone resist (495PMMA A Resists, solids: 7% in Anisole) was spin-coated on a 2-inch Si(100) wafer and baked for 45 min at 160 °C. The sample was exposed at 10 nA with a dose of 1300 μC cm^{-2}, developed for 45 s in a solution of methyl-isobutyl-ketone and isopropanol (mixture 1:3), rinsed in isopropanol and gently dried with pure nitrogen gas. The pattern was transferred by reactive ion etching using a SF$_6$/CHF$_3$ gas mixture.

The antisticking treatment was performed using 1H,1H,2H,2H-perfluorooctyltriethoxysilane (POTS) by chemical vapor deposition method. A sealed glass Petri dish containing the silicon master and several drops of POTS was heated in an oven at about 120 °C for 1 h to enable the reaction between the OH groups on the Si substrate surfaces and the POTS and then maintained at about 150 °C for 2 h to remove the unreacted POTS molecules.

A bilayer hard-PDMS/PDMS stamp was then replicated first by spin-coating a thin hard-PDMS layer on the silicon master and second by casting a mixture of commercial available (RTV615 from GE) two components solution (1:10) on top. The bilayer hard-PDMS/PDMS stamp was degassed and soft-baked at 60 °C for 48 h. Finally, after being peeled off from the silicon master, the bilayer stamp was treated with methyltrichlorosilane.

Imprinting: PDMS mold was placed under vacuum for 30 min. The silicon wafer was cleaned with ethanol solution and oxygen plasma. The silicon substrate was coated with iridium or ruthenium solution via dip-coating. Dip-coating was performed in a closed chamber with controlled atmosphere at relative humidity <10% and room temperature. The process consisted of i) dipping the substrate into the tank, ii) letting it immersed for 3 s, iii) withdrawing at speed of 10 mm s^{-1}, and iv) letting it in the close chamber for 1 min to allow complete evaporation of the solvent. Just after the deposition, the PDMS mold was applied on silicon surface and it was placed in oven at 130 °C for 5 min.[43] The PDMS mold was then removed and the film was calcined at 300 °C under nitrogen.

In Situ X-Ray Diffraction: The in situ XRD measurements at different temperatures were carried out using a Panalytical X'pert pro diffractometer equipped with a Co anode (λKα = 1.79031 Å) and a multichannel X'celerator detector. Each pattern was recorded in the θ–θ Bragg–Brentano geometry in the 15–120° 2θ range (during 40 s each 0.0334°). The high temperature oven chamber was an Anton Paar HTK 1200N and the crucible was made of alumina. The rise in temperature was between 25 and 400 °C, with a measurement every 50 °C. The nonindexed peaks corresponded to the substrate. The intensity of these peaks intensity increased with the temperature. This effect was already observed in other in situ XRD studies. This modification was attributed to the fact that, during the annealing, the amount of matter present on the film decreased(H$_2$O loss, polymer decomposition, Cl departure). Consequently, the contribution of the substrate to the diffraction signal became more important.

In Situ Infrared Ellipsometry: The films were analyzed by a Woolam ellipsometer IR-VASE equipped with a thermal environmental chamber. The measurements cover the spectral range from 1.7 to 30 microns (333–5900 wavenumbers) and were acquired every 25 °C.

In Situ Grazing-Incidence Small-Angle X-Ray Scattering and Wide-Angle X-Ray Scattering: In situ time-resolved GISAXS/WAXS were performed at the Austrian SAXS beamline at the ELETTRA synchrotron in Trieste (Italy) at a photon energy of 8 keV.[44] The beam size was set to 1 × 0.2 mm^2 (HxV). SAXS images were collected in grazing incidence (0.236°) using Pilatus3 1M detector (Dectris AG, Switzerland) at a distance of 1942.3 mm from the sample, with 30 s intervals between each frame. WAXS diffraction patterns were collected simultaneously with Pilatus 100K detector placed 197.6 mm from the sample. The patterns were corrected for the fluctuations of the primary intensity.[45] The domed hot stage (DHS1100, Anton Paar, Austria) was used for in situ temperature studies.

Microscopy: SEM imaging was performed on a SU-70 Hitachi FESEM. Voltage acceleration setup was 5 kV and usually upper detector was used for secondary electron acquisition. The surface morphology of the nanoimprinted films was also studied using an AFM Nanosurf C3000 equipment. Height images and profiles were recorded on 10 μm^2 area

Catalytic H$_2$ Generation: For the catalytic test in the batch reactor, NaBH$_4$ (Sigma Aldrich, 98% purity) was dissolved in NaOH (4 wt% solution) to obtain 4 wt% sodium borohydride solution. The solution was placed in glass reactor with two necks. H$_2$ production was probed with Bonkhorst flow meter. For the test performed in the microfluidic reactor, a photosensitive resin (AZ P4620 Photoresist, purchased Merk Performance Materials) was applied by spin coating (3000 rpm, 30 s)

on silicon wafer. Selective patterning was carried by photolithography by using a mask-less SmartPrint device (Smart Forces Technologies). After development, the photoresist was baked for hardening at 130 °C for 2 h before molding with PDMS and placed at 130 °C for 15 min for hardening. The PDMS microchannel was bonded on the glass substrate after activating the surface by a plasma treatment of 15 min.

Supporting Information

Supporting Information is available from the Wiley Online Library or from the author.

Conflict of Interest

The authors declare no conflict of interest.

Data Availability Statement

Research data are not shared.

[1] R. J. Seymour, J. O'Farrelly, in *Kirk-Othmer Encyclopedia of Chemical Technology*, **2012**, p. 1, https://onlinelibrary.wiley.com/action/showCitFormats?doi=10.1002%2F0471238961.1612012019052513.a01.pub3.

[2] M. Odziomek, M. Bahri, C. Boissière, C. Sanchez, B. Lassalle-Kaiser, A. Zitolo, O. Ersen, S. Nowak, C. Tard, M. Giraud, M. Faustini, J. Peron, *Mater. Horiz.* **2020**, *7*, 541.

[3] P. B. Kettler, *Org. Process Res. Dev.* **2003**, *7*, 342.

[4] T. Reier, M. Oezaslan, P. Strasser, *ACS Catal.* **2012**, *2*, 1765.

[5] a) M. Ming, Y. Zhang, C. He, L. Zhao, S. Niu, G. Fan, J.-S. Hu, *Small* **2019**, *15*, 1903057; b) H. Wang, H. D. Abruña, *ACS Catal.* **2019**, *9*, 5057.

[6] H.-I. Ryoo, J. S. Lee, C. B. Park, D.-P. Kim, *Lab Chip* **2011**, *11*, 378.

[7] K. C. Basavaraju, S. Sharma, R. A. Maurya, D. P. Kim, *Angew. Chem.* **2013**, *125*, 6867.

[8] A. M. Watson, X. Zhang, R. Alcaraz de la Osa, J. M. Sanz, F. González, F. Moreno, G. Finkelstein, J. Liu, H. O. Everitt, *Nano Lett.* **2015**, *15*, 1095.

[9] a) L. G. Wen, C. Adelmann, O. V. Pedreira, S. Dutta, M. Popovici, B. Briggs, N. Heylen, K. Vanstreels, C. J. Wilson, S. Van Elshocht, in *2016 IEEE Int. Interconnect Technology Conf./Advanced Metallization Conf. (IITC/AMC)*, IEEE, Piscataway, NJ **2016**; b) T. N. Arunagiri, Y. Zhang, O. Chyan, M. El-Bouanani, M. J. Kim, K. H. Chen, C. T. Wu, L. C. Chen, *Appl. Phys. Lett.* **2005**, *86*, 083104.

[10] A. C. Probst, T. Döhring, M. Stollenwerk, M. Wen, L. Proserpio, in *Int. Conf. on Space Optics—ICSO 2016*, SPIE, Bellingham, WA **2017**.

[11] A. Mallavarapu, P. Ajay, C. Barrera, S. V. Sreenivasan, *ACS Appl. Mater. Interfaces* **2021**, *13*, 1169.

[12] a) R. Glass, M. Möller, J. P. Spatz, *Nanotechnology* **2003**, *14*, 1153; b) J. Chai, F. Huo, Z. Zheng, L. R. Giam, W. Shim, C. A. Mirkin, *Proc. Natl. Acad. Sci. USA* **2010**, *107*, 20202; c) L. Huang, P.-C. Chen, M. Liu, X. Fu, P. Gordiichuk, Y. Yu, C. Wolverton, Y. Kang, C. A. Mirkin, *Proc. Natl. Acad. Sci. USA* **2018**, *115*, 3764; d) L. Huang, H. Lin, C. Y. Zheng, E. J. Kluender, R. Golnabi, B. Shen, C. A. Mirkin, *J. Am. Chem. Soc.* **2020**, *142*, 4570; e) L. Chen, X. Wei, X. Zhou, Z. Xie, K. Li, Q. Ruan, C. Chen, J. Wang, C. A. Mirkin, Z. Zheng, *Small* **2017**, *13*, 1702003; f) R. Guo, Y. Yu, Z. Xie, X. Liu, X. Zhou, Y. Gao, Z. Liu, F. Zhou, Y. Yang, Z. Zheng, *Adv. Mater.* **2013**, *25*, 3343; g) Y. Yu, X. Xiao, Y. Zhang, K. Li, C. Yan, X. Wei, L. Chen, H. Zhen, H. Zhou, S. Zhang, *Adv. Mater.* **2016**, *28*, 4926; h) Y. Yu, C. Yan, Z. Zheng, *Adv. Mater.* **2014**, *26*, 5508.

[13] a) B. Jiang, C. Li, M. Imura, J. Tang, Y. Yamauchi, *Adv. Sci.* **2015**, *2*, 1500112; b) C. Li, Ö. Dag, T. D. Dao, T. Nagao, Y. Sakamoto, T. Kimura, O. Terasaki, Y. Yamauchi, *Nat. Commun.* **2015**, *6*, 1; c) G. S. Attard, P. N. Bartlett, N. R. B. Coleman, J. M. Elliott, J. R. Owen, J. H. Wang, *Science* **1997**, *278*, 838.

[14] a) L. Longenberger, G. Mills, *J. Phys. Chem.* **1995**, *99*, 475; b) T. Sakai, P. Alexandridis, *J. Phys. Chem. B* **2005**, *109*, 7766; c) T. Sakai, Y. Horiuchi, P. Alexandridis, T. Okada, S. Mishima, *J. Colloid Interface Sci.* **2013**, *394*, 124; d) P. Alexandridis, *Chem. Eng. Technol.* **2011**, *34*, 15; e) M. Faustini, L. Nicole, E. Ruiz-Hitzky, C. Sanchez, *Adv. Funct. Mater.* **2018**, *28*, 1704158.

[15] T. Sakai, P. Alexandridis, *Langmuir* **2004**, *20*, 8426.

[16] M. Grobis, C. Schulze, M. Faustini, D. Grosso, O. Hellwig, D. Makarov, M. Albrecht, *Appl. Phys. Lett.* **2011**, *98*, 192504-1.

[17] V. Neu, C. Schulze, M. Faustini, J. Lee, D. Makarov, D. Suess, S. K. Kim, D. Grosso, L. Schultz, M. Albrecht, *Nanotechnology* **2013**, *24*, 145702-1.

[18] M. Gayrard, J. Voronkoff, C. Boissière, D. Montero, L. Rozes, A. Cattoni, J. Peron, M. Faustini, *Nano Lett.* **2021**, *21*, 2310.

[19] M. Faustini, B. Marmiroli, L. Malfatti, B. Louis, N. Krins, P. Falcaro, G. Grenci, C. Laberty-Robert, H. Amenitsch, P. Innocenzi, D. Grosso, *J. Mater. Chem.* **2011**, *21*, 3597.

[20] M. Faustini, D. Grosso, *C. R. Chim.* **2016**, *19*, 248.

[21] a) M. Kuemmel, J. Allouche, L. Nicole, C. Boissière, C. Laberty, H. Amenitsch, C. Sanchez, D. Grosso, *Chem. Mater.* **2007**, *19*, 3717; b) M. Kuemmel, J.-H. Smått, C. Boissière, L. Nicole, C. Sanchez, M. Lindén, D. Grosso, *J. Mater. Chem.* **2009**, *19*, 3638.

[22] M. Faustini, G. L. Drisko, A. A. Letailleur, R. S. Montiel, C. Boissière, A. Cattoni, A. M. Haghiri-Gosnet, G. Lerondel, D. Grosso, *Nanoscale* **2013**, *5*, 984.

[23] E. Bindini, G. Naudin, M. Faustini, D. Grosso, C. Boissière, *J. Phys. Chem. C* **2017**, *121*, 14572.

ADVANCED
SCIENCE NEWS
www.advancedsciencenews.com

NANO · MICRO
small
www.small-journal.com

[24] F. T. L. Muniz, M. A. R. Miranda, C. Morilla dos Santos, J. M. Sasaki, *Acta Crystallogr., Sect. A: Found. Adv.* **2016**, *72*, 385.

[25] R. M. Silverstein, G. C. Bassler, *J. Chem. Educ.* **1962**, *39*, 546.

[26] K. Pielichowski, K. Flejtuch, *J. Anal. Appl. Pyrolysis* **2005**, *73*, 131.

[27] a) X.-M. Li, H.-L. Liu, X. Liu, N. Fang, X.-H. Wang, J.-H. Wu, *Sci. Rep.* **2015**, *5*, 1; b) B. Jiang, C. Li, Ö. Dag, H. Abe, T. Takei, T. Imai, M. S. A. Hossain, M. T. Islam, K. Wood, J. Henzie, *Nat. Commun.* **2017**, *8*, 1.

[28] E. Cariati, C. Dragonetti, D. Roberto, R. Ugo, E. Lucenti, *Inorg. Chim. Acta* **2003**, *349*, 189.

[29] R. Psaro, D. Roberto, R. Ugo, C. Dossi, A. Fusi, *J. Mol. Catal.* **1992**, *74*, 391.

[30] a) C. P. Booker, J. T. Keiser, *J. Phys. Chem.* **1989**, *93*, 1532; b) M. I. Zaki, B. Tesche, L. Kraus, H. Knözinger, *Surf. Interface Anal.* **1988**, *12*, 239.

[31] a) J. T. Yates Jr., K. Kolasinski, *J. Chem. Phys.* **1983**, *79*, 1026; b) D. I. Kondarides, Z. Zhang, X. E. Verykios, *J. Catal.* **1998**, *176*, 536.

[32] M. Faustini, A. Grenier, G. Naudin, R. Li, D. Grosso, *Nanoscale* **2015**, *7*, 19419.

[33] R. Li, M. Boudot, C. Boissière, D. Grosso, M. Faustini, *ACS Appl. Mater. Interfaces* **2017**, *9*, 14093.

[34] A. Guiet, T. Reier, N. Heidary, D. Felkel, B. Johnson, U. Vainio, H. Schlaad, Y. Aksu, M. Driess, P. Strasser, *Chem. Mater.* **2013**, *25*, 4645.

[35] C. Luo, X. Ni, L. Liu, S. i. M. Nomura, Y. Chen, *Biotechnol. Bioeng.* **2010**, *105*, 854.

[36] H.-L. Chen, A. Cattoni, R. De Lépinau, A. W. Walker, O. Höhn, D. Lackner, G. Siefer, M. Faustini, N. Vandamme, J. Goffard, *Nat. Energy* **2019**, *4*, 761.

[37] a) A. Cattoni, P. Ghenuche, A.-M. Haghiri-Gosnet, D. Decanini, J. Chen, J.-L. Pelouard, S. p. Collin, *Nano Lett.* **2011**, *11*, 3557; b) T. Bottein, O. Dalstein, M. Putero, A. Cattoni, M. Faustini, M. Abbarchi, D. Grosso, *Nanoscale* **2018**, *10*, 1420.

[38] O. Dalstein, D. R. Ceratti, C. Boissière, D. Grosso, A. Cattoni, M. Faustini, *Adv. Funct. Mater.* **2016**, *26*, 81.

[39] H. N. Abdelhamid, *Int. J. Hydrogen Energy* **2020**, *46*, 726.

[40] Y. Shang, R. Chen, *Energy Fuels* **2006**, *20*, 2149.

[41] D.-H. Ko, W. Ren, J.-O. Kim, J. Wang, H. Wang, S. Sharma, M. Faustini, D.-P. Kim, *ACS Nano* **2016**, *10*, 1156.

[42] M. Faustini, J. Kim, G.-Y. Jeong, J. Y. Kim, H. R. Moon, W.-S. Ahn, D.-P. Kim, *J. Am. Chem. Soc.* **2013**, *135*, 14619.

[43] M. Faustini, A. Cattoni, J. Peron, C. Boissière, P. Ebrard, A. Malchère, P. Steyer, D. Grosso, *ACS Nano* **2018**, *12*, 3243.

[44] H. Amenitsch, M. Rappolt, M. Kriechbaum, H. Mio, P. Laggner, S. Bernstorff, *J. Synchrotron Radiat.* **1998**, *5*, 506.

[45] M. Burian, C. Meisenbichler, D. Naumenko, H. Amenitsch, *arXiv:2007.02022* **2020**.